Monthly Notices
of the
ROYAL ASTRONOMICAL SOCIETY

MNRAS **488,** 720–727 (2019)
Advance Access publication 2019 June 28

doi:10.1093/mnras/stz1774

Spectro-timing analysis of MAXI J1535–571 using *AstroSat*

Yash Bhargava [1]★ Tomaso Belloni,[2] Dipankar Bhattacharya[1] and Ranjeev Misra[1]

[1]*Inter-University Centre for Astronomy and Astrophysics, Post Box No. 4, Ganeshkhind, Pune-411007, India*
[2]*INAF, Osservatorio Astronomico di Brera, Via E. Bianchi 46, I-23807 Merate (LC), Italy*

Accepted 2019 June 25. Received 2019 June 12; in original form 2019 January 11

ABSTRACT

We report the results of the analysis of an *AstroSat* observation of the black hole candidate MAXI J1535–571 during its hard-intermediate state. We studied the evolution of the spectral and timing parameters of the source during the observation. The observation covered a period of ∼5 d and consisted of 66 continuous segments, corresponding to individual spacecraft orbits. Each segment was analysed independently. The source count rate increased roughly linearly by ∼30 per cent. We modelled the spectra as a combination of radiation from a thermal disc component and a power law. The timing analysis revealed the presence of strong quasi-periodic oscillations with centroid frequency $\nu_{\rm QPO}$ fluctuating in the range of 1.7–3.0 Hz. We found a tight correlation between the QPO centroid frequency $\nu_{\rm QPO}$ and the power-law spectral index Γ, while $\nu_{\rm QPO}$ appeared not to be correlated with the linearly increasing flux itself. We discuss the implications of these results on physical models of accretion.

Key words: accretion, accretion discs – black hole physics – X-rays: binaries.

1 INTRODUCTION

Black hole binaries (BHBs) are stellar systems in which one of the objects is a stellar-mass black hole (BH) and the companion star is typically a low-mass star that fills its Roche lobe, leading to accretion of matter on to the BH, or a high-mass star feeding the BH through its stellar wind. The majority of these systems are transient, with only a few known persistent sources. The evolution of their properties, in particular during transient outbursts when the accretion rate swing is large, is characterized by a series of source states, defined through the spectral and fast-variability properties (see Done, Gierliński & Kubota 2007; Belloni 2010; Belloni, Motta & Muñoz-Darias 2011). The BHBs typically follow a hysteresis loop in the hardness–intensity diagram (HID), and different positions on this diagram correspond to different states of the system. The low hard state (LHS) of the system is characterized by a hard spectrum and high fractional rms variability (∼30 per cent; Belloni 2005). As the source evolves into a hard-intermediate state (HIMS), the spectrum of the source softens and indicates the presence of a thermalized disc. Low-frequency quasi-periodic oscillations (QPOs) of type C are also detected in these states (Casella, Belloni & Stella 2005). The source can then evolve into a soft-intermediate state (SIMS) which is characterized by a softer spectrum with the disc component dominating the flux. Transient QPOs of Types A and B are also seen in the power spectrum from this state (Casella et al. 2005). The source then typically evolves into a high soft state (HSS) in which the spectrum is strongly dominated by a thermalized disc. The power spectrum can be fitted with a flat power law. The source typically fades and returns to the LHS.

QPOs are ubiquitous features in the variability pattern of BHB systems (see Belloni & Stella 2014, and references therein). Low-frequency QPOs (0.1–30 Hz) are associated with oscillations in the inner regions of the accretion disc. They are observed in the hard states, LHS and HIMS. Their energy spectrum indicates that their origin is connected to the high-energy component and not the thermal disc component. As their frequency is too low to be directly associated with Keplerian motion in the inner region of the accretion flow, models have concentrated on other physical time-scales. The RPM model (Stella & Vietri 1998; Stella, Vietri & Morsink 1999) associates these oscillations to the Lense–Thirring precession frequency at a certain radius of the accretion flow. A more complex model connected to accretion has been proposed, which takes into account a broader precessing region surrounded by a thermal disc (Ingram & Done 2011; Ingram 2016, and references therein), as in the truncated-disc paradigm (see Done et al. 2007). The study of the correlation between spectral and timing properties can help in constraining the theoretical models of accretion discs around a BH. In particular, the dependence of the QPO centroid frequency on spectral parameters is a crucial observable. A deep study of the correlation between QPO centroid frequency ($\nu_{\rm QPO}$) and slope of the high-energy power law (Γ) for the peculiar system GRS 1915+105 was conducted by Vignarca et al. (2003). In this work, the authors extract and present this correlation also for other systems (GRO J1655-40, XTE J1550-564, XTE J1748-288, and 4U 1630-47), showing that it is a general property for BHBs. The correlation is a positive one: higher QPO frequencies are associated with steeper energy spectra and a turn-off at high frequencies is

★ E-mail: yash@iucaa.in

observed. This work and subsequent works by Shaposhnikov & Titarchuk (2007) and Shaposhnikov & Titarchuk (2009) sample two different regimes of variations in the parameters: for GRS 1915+105 fast variations, within an hour, are considered, while for the other more conventional transient systems like Cygnus X-1 the values come from observations spread throughout an outburst, i.e. months.

MAXI J1535–571 was discovered independently by MAXI and *Swift*-BAT on 2017 September 2 (Markwardt et al. 2017; Negoro et al. 2017a). Kennea et al. (2017) provided a more accurate position of the source using *Swift*-UVOT and *Swift*-XRT observations. Scaringi & ASTR211 Students (2017) reported the detection of an optical counterpart to MAXI J1535–571, followed by the detection of near-infrared radiation by Dincer (2017). Radio detection from *ATCA* (Russell et al. 2017) and further brightening in the X-ray flux (Negoro et al. 2017b) suggested the nature of the compact object as a BH. Mereminskiy & Grebenev (2017) detected low-frequency QPOs at 1.9 Hz in *Swift*-XRT observations conducted on 2018 September 11, indicating that the source was in the HIMS, i.e. in transition from the hard to soft states. Mereminskiy et al. (2018) and Stiele & Kong (2018) discuss the evolution of the QPO frequency and observe a positive correlation between the QPO centroid frequency and the power-law index of the spectrum, relating the QPO centroid frequency to the inner truncation radius of the disc, Mereminskiy et al. (2018) derive self-consistent results for the physical parameters of the inner Comptonizing cloud. Xu et al. (2018) analyse the *NuSTAR* spectrum and constrain the spin of the BH to >0.84 and inner truncation radius to $<2.01\ R_{\rm ISCO}$. Sreehari et al. (2019) and Sridhar et al. (2019) analyse the spectral properties of the source using the data from the *AstroSat* observation and constrain the mass of the source to 5.14–7.83 $M_\odot$ and $10.39^{+0.61}_{-0.62}\ M_\odot$, respectively. Sreehari et al. (2019) also present the evolution of the timing parameters using *Swift*-XRT and LAXPC observations and classify the states of the source using the QPOs detected in in the power spectra.

In this paper, we report the result of the spectral-timing analysis of the *AstroSat* SXT+LAXPC data of MAXI J1535–571 obtained over a period of five days and concentrate on the $\nu_{\rm QPO}$–Γ correlation.

2 OBSERVATION AND DATA ANALYSIS

Based on a trigger from Negoro et al. (2017a), *AstroSat* (Singh et al. 2014) triggered a Target of Opportunity (ToO) observation (Observation ID: 01536) of MAXI J1535–571 from 2017 September 12 (MJD 58008.2309) to 2017 September 17 (MJD 58013.1545). The source was observed in the rising part of the outburst. In order to place the *AstroSat* data in the context of the outburst, we analysed data from the Neutron star Interior Composition Explorer (NICER) mission on board the International Space Station (Gendreau, Arzoumanian & NICER Team 2017a), which observed the target regularly over the period 2017 September 9 to October 11 and provided a good picture of the overall evolution of the first part of the outburst. We extracted the NICER count rates from all detectors without background subtraction, since the source is very bright and produced light curves in different energy bands as well as hardness ratios. In Fig. 1, we show the NICER light curves in the full 0.3–10 keV energy band (top panel) and in the 5–10 keV energy band, closest to the LAXPC coverage. The grey band in the figure represents the time interval of the *AstroSat* observation. It is clear that *AstroSat* observed during an interval of roughly monotonic rise of flux in the 5–10 keV band, while the full NICER light curve is more complex and in particular shows a faster flux

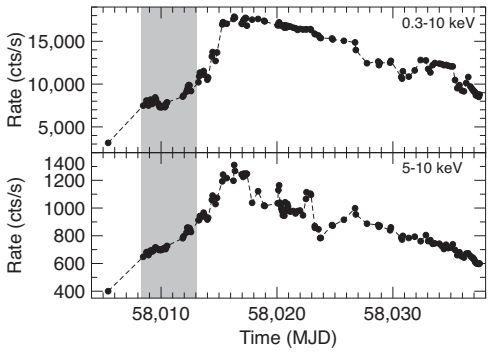

Figure 1. NICER light curves of MAXI J1535–571 (top panel: 0.3–10 keV, bottom panel: 5–10 keV) over the period 2017 September 9 to October 11, with the time interval of the *AstroSat* observation marked in grey.

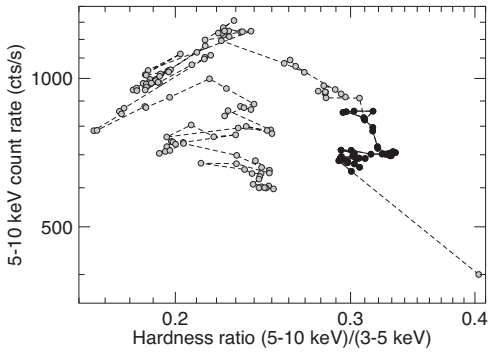

Figure 2. HID of MAXI J1535–571 as observed by NICER over the same interval as Fig. 1. The energy bands for the two axes are indicated in the label. The black points are those within the observation window of *AstroSat*. The dashed lines mark a longer time gap (see Fig. 1).

increase after the *AstroSat* coverage. The HID from the NICER data, a useful tool to represent the evolution of a BH transient (see e.g. Belloni et al. 2011), is shown in Fig. 2, where the points covering the *AstroSat* observation period are marked in black. The typical counterclockwise evolution can be seen (Belloni et al. 2011), but in order to fully classify the source states additional timing analysis needs to be done (see below).

Primary instruments on board *AstroSat* which observed the outburst include the Soft X-ray Telescope (SXT) and the Large Area X-ray Proportional Counter (LAXPC). SXT is a focussing X-ray telescope that operates in the energy range of 0.3–8 keV with an energy resolution of 5–6 per cent at 1.5 keV and an effective area of $\sim$128 cm^2 at 1.5 keV (Singh et al. 2017). The observation of the source was carried out with SXT operating in fast window (FW) timing mode. This mode observes only the central 150 × 150 pixels from the total 600 × 600 pixels. Due to the large point spread function of SXT, the source occupied the complete field of view (FOV; 10 arcmin) in FW mode. However, the smaller number of pixels to be read out allowed a better time resolution (0.278 s) than the full-frame read-out (2.37 s)

LAXPC is an X-ray proportional counter array operating in the range of 3–80 keV with an energy resolution of 10–15 per cent at 20 keV. The timing resolution of the instrument is 10 μs with a dead time of 42 μs. There are three identical detectors (referred to as LXP10, LXP20, and LXP30, respectively) on *AstroSat* with a combined effective area of 6000 cm^2 (Yadav et al. 2016; Antia et al. 2017). LAXPC was operated in event analysis mode for the

duration of the observation, which allowed for the data of individual photons to be available to the user.

2.1 Data reduction

The data reduction of the *AstroSat* observation was done using the instrument pipelines provided by the respective payload operation centres (POCs). SXT data were reduced using SXT pipeline `AS1SXTLevel2 -1.4 a` and the calibration files released with the pipeline. LAXPC data were reduced using the LAXPC pipeline `laxpc_make_event` from the package `laxpcsoft_Sep12_2017`. The package also includes the calibration files for all the units of LAXPC.

To monitor the evolution of the source over the observation period, we divided the observation into the 66 *AstroSat* orbits, which are separated by gaps due to Earth occultations and passage through the South Atlantic Anomaly (SAA). This resulted in 66 data segments roughly equally spaced and with comparable exposures. The brightness of the source allowed us to analyse the spectral and timing properties for each of the segments, as each segment had a large number of source photons. The segment boundaries are listed in Table 1. Standard Good time intervals (GTIs) were applied to each of the segments to remove the section corresponding to occultation of the source by Earth and near the SAA region. The GTI were created using the tool `laxpc_make_stdgti` provided by the LAXPC POC. Some intervals showed count-rate dips that were identified as instrumental and removed. The orbit-wise data from SXT were merged using the `sxtevtmerger` tool provided by the SXT POC. The individual segments were extracted using `xselect` (HEASOFT version 6.23) on the merged event file and the GTI used for LAXPC. For each orbit of *AstroSat* the SXT has a lower exposure than LAXPC due to additional constraints (including reflection from the earth, larger SAA window). Due to the jitter in satellite pointing, the SXT coverage is also lower as the source occasionally moved out of the reduced window used in the FW mode.

2.2 Spectral analysis

The spectra for all the segments were extracted using `xselect` for SXT and `laxpc_make_spectra` for LAXPC. As the observation was conducted with the SXT operating in FW mode, all the photons observed by SXT were assumed to be from the source. The spectra from the LAXPC were extracted for all instrument layers. However, due to a gas leak in LXP30, the response of the detector is considered uncertain and thus the data from this unit were not used for the spectral analysis, while they were retained for timing analysis. For the SXT, as advised by the POC, standard response, ancillary response, and background files were used for the analysis. In the case of the LAXPC, the responses were selected based on the spectral extraction and the background was modelled from the nearest blank-sky observation that had similar satellite position as the current observation.

The background estimates for both LXP10 and LXP20 are somewhat uncertain, so the spectra beyond 30 keV (where background starts dominating over the source) were ignored for the analysis. The response matrix modelling of SXT is uncertain below 0.8 keV due to the lack of a suitable calibration source. In our case, the source is brighter than the Crab and thus magnifies unmodelled instrumental features below 1 keV. Therefore, the data below 1 keV were ignored. To use the χ^2 statistics in judging the quality of the model to explain the data, we grouped the data from SXT such that each energy bin has at least 20 counts. The LAXPC has sufficient counts in each energy bin to allow for the χ^2 statistics but the rebinning of the channels was done logarithmically, keeping dE/E at 5 per cent to account for the coarser energy resolution of the instrument. To account for the uncertainties in the response of the instruments a 3 per cent systematic error was added to the model.

Spectral analysis of *NuSTAR* data of MAXI J1535–571 by Xu et al. (2018) indicates that the underlying compact object is a BH candidate. The authors have modelled the spectra by a thermal disc that is illuminated by a lamp post corona situated at $h = 7.2^{+0.8}_{-2.0}\, r_g$. The authors also report that the source has a particularly high absorption column density ($N_H \sim 8.2^{+0.3}_{-0.6} \times 10^{22}$ cm^{-2}). This value is slightly higher than the value reported in the preliminary analyses by Kennea (2017) (*Swift*-XRT; $N_H \sim 3.6 \pm 0.2 \times 10^{22}$ cm^{-2}) and by Gendreau et al. (2017b) (NICER; $N_H \sim 4.89 \pm 0.06 \times 10^{22}$ cm^{-2}). Xu et al. (2018) have attributed this to the inclusion of the thermal disc in their modelling of the spectra. The observations from these different instruments were conducted at different epochs and thus the variation in the observed absorption could be due to internal changes in the source.

In this work, we modelled the source spectrum using a thermal disc and a power-law component. We did not find a significant presence of the Fe K α fluorescence line. Using the phenomenological model of Xu et al. (2018) for the iron line and response matrices of SXT and LAXPC, we simulated a spectrum for the exposure of a typical segment. We find that the iron line was not required to have an acceptable fit to the simulated spectrum. Thus, we claim that the iron line cannot be detected at a significant level for an exposure of the typical segment. We find a strong iron line when the spectra of all the segments are combined, the analysis of which will be reported in a future work. The absorption column density was modelled by `TbAbs` with the abundances from Wilms, Allen & McCray (2000) and the cross-sections from Verner et al. (1996). The model provided a satisfactory fit to the data with a typical reduced chi squared value of 1.1 for ~700 deg of freedom. A typical spectrum and the residuals to the fitted model is shown in Fig. 3. The time evolution of the best-fittng parameters is shown in Fig. 4. The absorption column density is around 5×10^{22} cm^{-2} for all the segments. Sreehari et al. (2019) and Sridhar et al. (2019) report a slightly lower value for the same observation. The difference in the N_H is arising due to a difference in the ancillary response file (ARF) of SXT used by different authors. Our analysis uses the default on-axis ARF provided with the official pipeline. The inner disc temperature stays roughly constant around the typical value of 0.2 keV. The power-law flux and the disc flux increase over the observation, but with significant fluctuations that appear to be correlated. Interestingly, the power-law index does not show a secular increase over the course of the observation.

2.3 Timing analysis

For each of the 66 segments, we produced power density spectra (PDSs) from intervals of 16.384 s and averaged them. The final PDSs were rebinned logarithmically before fitting. The PDSs were extracted using the General High-energy Aperiodic Timing Software (GHATS version 1.1.1).[1] All the PDSs display a clear QPO with harmonically related peaks. An example of a PDS is shown in Fig. 5. The PDSs were fitted with a model consisting of multiple Lorentzians: two flat-top components for the band-limited noise,

[1]The software can be downloaded from http://www.brera.inaf.it/utenti/belloni/GHATS/Home.html. The software is written by TMB.

Table 1. List of start and end points of the segments of the data. The time stamps are measured from MJD 58008.24759259 in seconds. The spectral and timing parameters with 90 per cent confidence interval for each of the segments are also tabulated. Due to jitter in the satellite, the pointing of SXT went off source for certain orbits due to which no SXT data was available for those segments. The spectral parameters could not be constrained for these segments and thus they have not been reported here.

Segment number	Start time[a] (s)	End time[a] (s)	Power-law index	QPO frequency (Hz)
1	0	3735.296	–	2.161 ± 0.006
2	3735.296	9777.92	2.380 ± 0.011	2.188 ± 0.004
3	9777.92	15622.784	2.416 ± 0.011	2.406 ± 0.006
4	15622.784	21468.8	2.438 ± 0.011	2.514 ± 0.007
5	21468.801	27314.048	2.450 ± 0.011	2.597 ± 0.008
6	27314.049	33160.064	2.474 ± 0.011	2.717 ± 0.006
7	33160.062	41366.911	2.468 ± 0.011	2.773 ± 0.013
8	41366.91	47638.911	2.468 ± 0.011	2.573 ± 0.009
9	47638.91	53910.911	2.423 ± 0.011	2.486 ± 0.001
10	53910.91	60166.529	2.408 ± 0.012	2.388 ± 0.006
11	60166.527	66405.759	–	2.753 ± 0.006
12	66405.758	72710.525	–	2.820 ± 0.006
13	72710.531	78982.525	2.449 ± 0.013	2.600 ± 0.005
14	78982.531	85254.525	2.415 ± 0.011	2.370 ± 0.006
15	85254.531	91526.915	2.384 ± 0.013	2.272 ± 0.004
16	91526.914	97453.697	2.439 ± 0.011	2.518 ± 0.004
17	97453.695	103283.329	2.453 ± 0.011	2.561 ± 0.007
18	103283.328	109129.345	2.491 ± 0.012	2.771 ± 0.004
19	109129.344	114975.361	2.447 ± 0.011	2.542 ± 0.006
20	114975.359	120823.806	2.432 ± 0.011	2.505 ± 0.005
21	120823.805	129158.915	2.400 ± 0.011	2.201 ± 0.010
22	129158.914	135430.915	2.357 ± 0.011	1.972 ± 0.008
23	135430.906	147942.525	2.313 ± 0.011	1.813 ± 0.007
24	147942.531	154230.915	–	1.792 ± 0.005
25	154230.906	160502.915	–	1.809 ± 0.005
26	160502.906	166774.915	2.332 ± 0.012	1.838 ± 0.005
27	166774.906	173046.915	2.325 ± 0.011	1.844 ± 0.005
28	173046.906	179269.759	2.305 ± 0.011	1.725 ± 0.004
29	179269.766	185114.618	2.312 ± 0.011	1.789 ± 0.004
30	185114.625	190944.634	2.359 ± 0.011	2.024 ± 0.004
31	190944.641	196807.04	2.360 ± 0.011	2.039 ± 0.005
32	196807.047	202653.056	2.344 ± 0.011	1.960 ± 0.006
33	202653.062	208485.884	2.349 ± 0.011	1.982 ± 0.005
34	208485.891	216951.29	2.385 ± 0.011	2.264 ± 0.012
35	216951.297	223223.29	2.425 ± 0.011	2.500 ± 0.007
36	223223.297	229446.15	2.446 ± 0.011	2.469 ± 0.010
37	229446.141	235718.15	2.405 ± 0.014	2.144 ± 0.007
38	235718.141	242023.29	–	2.381 ± 0.006
39	242023.297	248295.29	–	2.124 ± 0.008
40	248295.297	254567.29	2.386 ± 0.011	2.129 ± 0.006
41	254567.297	260839.29	2.388 ± 0.011	2.113 ± 0.004
42	260839.297	266931.072	2.371 ± 0.011	2.039 ± 0.004
43	266931.062	272775.947	2.409 ± 0.011	2.251 ± 0.010
44	272775.938	278621.197	2.426 ± 0.011	2.311 ± 0.005
45	278621.188	284467.572	2.415 ± 0.011	2.290 ± 0.009
46	284467.594	290313.603	2.406 ± 0.011	2.252 ± 0.006
47	290313.594	296157.322	2.398 ± 0.011	2.235 ± 0.008
48	296157.312	298470.915	–	2.261 ± 0.010
49	298470.906	304742.915	2.399 ± 0.011	2.150 ± 0.008
50	304742.906	311014.915	2.369 ± 0.011	2.005 ± 0.005
51	311014.906	317237.759	2.399 ± 0.011	2.167 ± 0.006
52	317237.75	323542.54	–	2.219 ± 0.008
53	323542.531	329814.54	–	2.178 ± 0.004
54	329814.531	336086.915	2.420 ± 0.014	2.284 ± 0.005
55	336086.906	342358.915	2.440 ± 0.011	2.373 ± 0.004
56	342358.906	348630.915	2.465 ± 0.011	2.531 ± 0.004
57	348630.906	354590.478	2.501 ± 0.011	2.755 ± 0.004
58	354590.469	360436.478	2.499 ± 0.011	2.740 ± 0.005
59	360436.469	366298.884	2.487 ± 0.011	2.657 ± 0.005
60	366298.875	372128.509	2.420 ± 0.011	2.254 ± 0.005
61	372128.5	377974.54	2.424 ± 0.011	2.302 ± 0.008

Table 1 *– continued*

Segment number	Start time[a] (s)	End time[a] (s)	Power-law index	QPO frequency (Hz)
62	377974.531	386263.29	2.440 ± 0.011	2.355 ± 0.012
63	386263.281	392535.29	2.418 ± 0.011	2.292 ± 0.008
64	392535.281	405030.134	2.404 ± 0.011	2.103 ± 0.005
65	405030.156	411334.915	–	2.196 ± 0.006
66	411334.906	417623.29	–	2.077 ± 0.006

[a]Measured from MJD 58008.24759259.

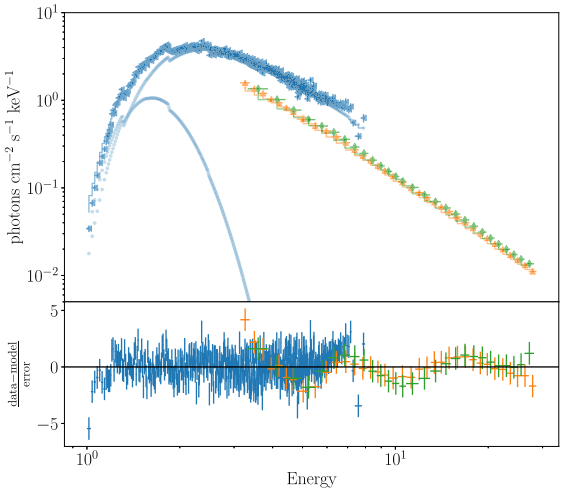

Figure 3. Typical energy spectrum of the source. The blue left triangles, orange up triangles, and green diamonds denote the spectrum observed by SXT, LXP10, and LXP20, respectively. Spectrum from SXT covers the energy range of 1–8 keV, while both LAXPC units cover 3.5–30 keV. The top panel shows the unfolded spectrum. The slight difference in the level of the SXT and LAXPC spectra is known to be due to systematic errors in the model of SXT ARF. To indicate the shape of the spectra, the data have been highly rebinned. The colour version of the figure is available in online version of the manuscript.

up to four harmonically related components for the QPO and its harmonics (sub-harmonic, fundamental, second harmonic, and third harmonic, of which only the fundamental and the second harmonic are always detected) and a broad component for the L_h feature (see Belloni, Psaltis & van der Klis 2002). In addition, a flat power-law component was added to fit the Poissonian noise contribution. The fits were limited to the 0.0625–300 Hz range.

Here, we focus on the centroid frequency of the QPO. The signal is so strong that its measurement is largely model independent. While the source count rate (and flux) increased roughly linearly throughout the observation, the QPO frequency varied in the 1.7–2.8 Hz range with no apparent correlation with the count rate. This can be seen clearly in Fig. 6. From the figure, one can see that the residuals from the linear fits to the two light curves are anticorrelated and that $\nu_{\rm QPO}$ seems to have an anticorrelation with the residuals of the 30–80 keV count rate (and hence a possible positive correlation with those of 3–10 keV). Comparing the bottom panels of Figs 4 and 6, we can see that the QPO frequency is indeed well correlated with the power-law photon index as determined from the combined SXT+LAXPC spectral fits. The correlation is very tight and can be seen in Fig. 7.

In order to put our results in a more general context of the outburst, we analysed the available NICER data of the rising part of the outburst of MAXI J1535–571, corresponding to the points

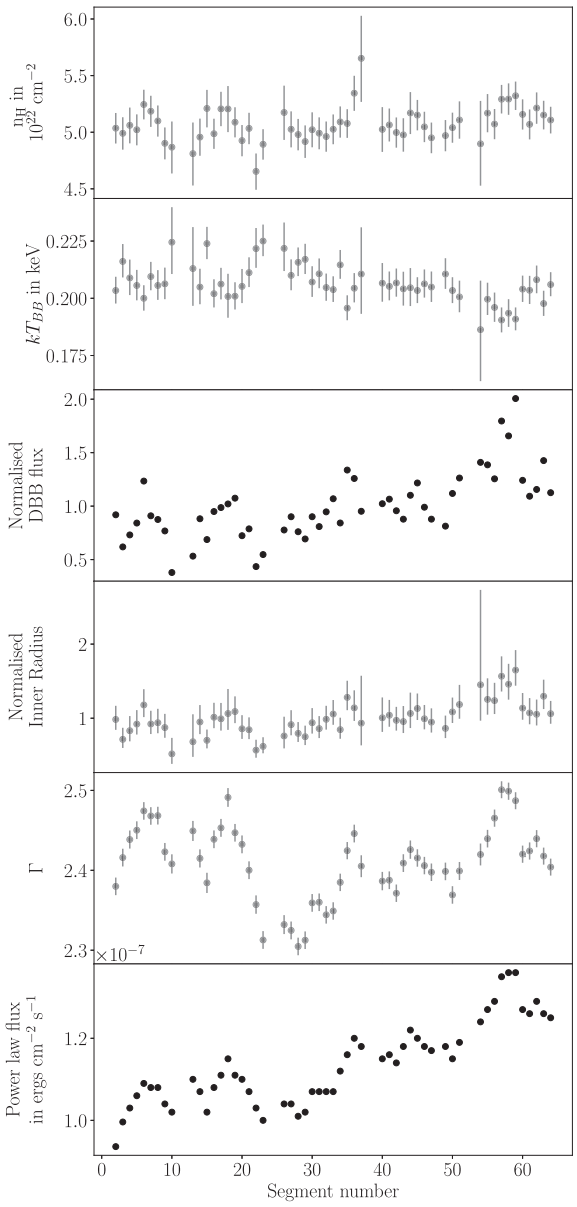

Figure 4. Time evolution of the best-fitting spectral parameters. In some of the segments, due to the satellite jitter, the source was outside the SXT field of view and thus no SXT spectra were available. The parameters for these segments could not be constrained well, and thus, they were excluded from further analysis and are not shown here. The disc flux is connected to the normalization of the component and is in arbitrary units.

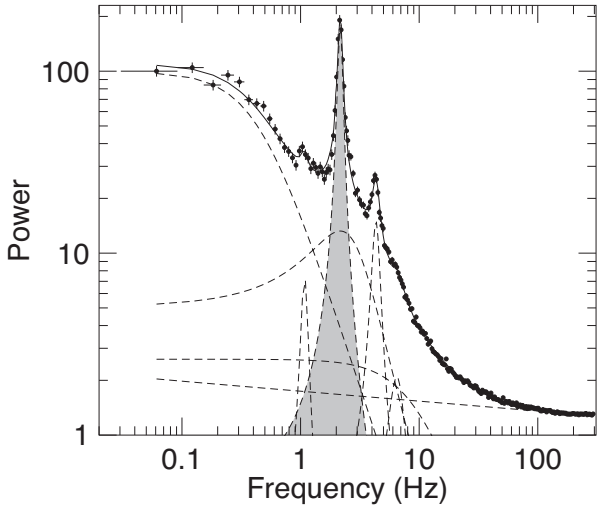

Figure 5. The PDS from the first segment. The thick line represents the best-fitting model and the dashed lines the different components. The QPO peak at the fundamental frequency is marked in grey.

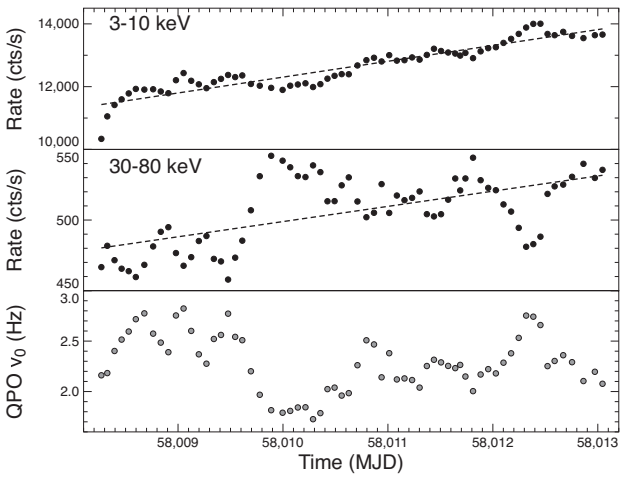

Figure 6. Top panel: LAXPC light curve in the 3–10 keV band with a linear fit. Middle panel: light curve in the 30–80 keV band with a linear fit. Bottom panel: time evolution of the centroid frequency of the QPO. Errors are present in all panels, but are smaller than the symbols.

in Fig. 1 before MJD 58015 (up to just before the large increase in count rate). The analysis was performed in the same way as described before for the *AstroSat* data using all available counts detected by NICER. The $\nu_{\rm QPO}$ was also very clear and easy to detect in the PDS despite the fact that the typical segment duration was ∼6 min. In Fig. 8, we plot the NICER $\nu_{\rm QPO}$ as a function of the NICER 5–10 keV rate, chosen in order to be close to the LAXPC energy band. The points corresponding to times overlapping with the *AstroSat* observing window are marked in black. One can see that the results are consistent for the overlapping period, with no correlation between frequency and count rate. However, after *AstroSat* stopped observing there is a clear positive correlation between the two parameters. Mereminskiy et al. (2018) and Stiele & Kong (2018) also perform a spectro-timing analysis of this source and observe a similar positive correlation between the $\nu_{\rm QPO}$ and power-law index. The extent of the observations analysed by these authors is larger

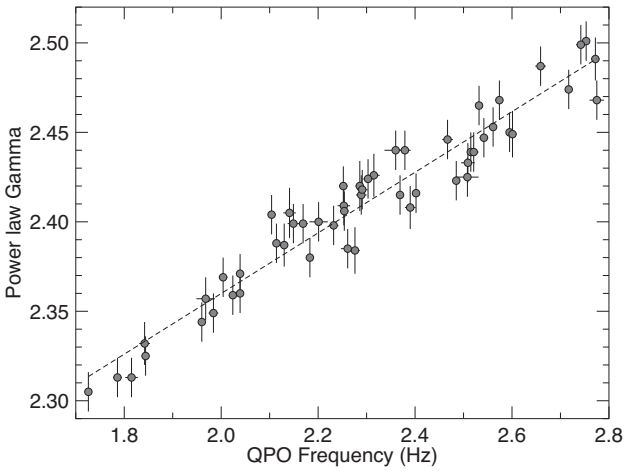

Figure 7. Correlation between power-law spectral index Γ and QPO centroid frequency $\nu_{\rm QPO}$. The line is the best-fitting linear correlation. The segments in which SXT data were not available are not included.

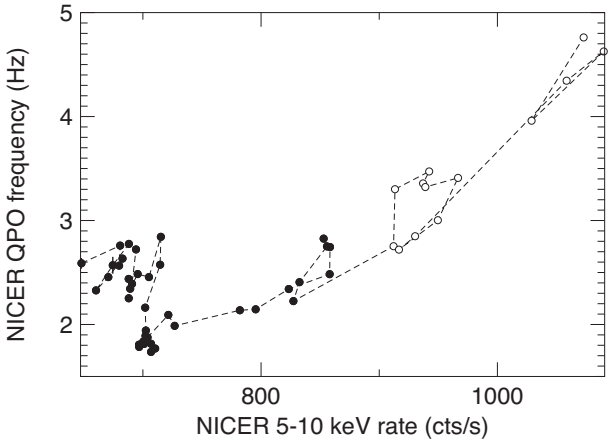

Figure 8. Correlation between QPO frequency and 5–10 keV count rate for the NICER data before MJD 58015 (before the peak of the outburst, see Fig. 1). The black points indicate observations within the *AstroSat* observing window.

than the *AstroSat* observation window and thus the tight correlation we observe is a sub-set of the correlation observed by them.

3 DISCUSSION

We have performed a spectro-timing analysis of the BHB MAXI J1535–571 using the observation conducted by *AstroSat* during the hard intermediate state of the source. The sources exhibit a secular roughly linear increase in the flux during the course of the observation. Fluctuations over the secular increase were observed in both softer and harder energy bands. The residuals from the linear fit for 3–10 keV and 30–80 keV are observed to be anticorrelated.

The energy spectrum of the source was modelled using an absorbed thermal disc blackbody with a power law as a non-thermal component. The high intrinsic absorption reported by Kennea (2017), Gendreau et al. (2017b), and Xu et al. (2018) is also seen in current observation. The disc temperature remains typically around 0.2 keV with significant deviations in some segments. The secular increase in the total flux reflects an increase in both the flux of the non-thermal and thermal components (see Fig. 4). The

power-law index of the hard component does not show a secular variation, but oscillates between 2.3 and 2.5, clearly being the cause of the anticorrelation in the residuals from the linear fits to the flux evolution in different bands. The oscillations are not random, but seem to follow a random walk around 2.4, with small variations between adjacent segments.

The PDS for individual segments show band-limited noise and a prominent QPO, with harmonics and sub-harmonics present in some of the segments. This shape of the PDS is typical of the HIMS (see Belloni et al. 2011). The centroid frequency of the QPO as a function of time (see Fig. 6) oscillates between 1.7 and 3.0 Hz and the oscillations follow those of the power-law index very closely (Fig. 7). The correlation for a larger observation window has been reported by Mereminskiy et al. (2018) and Stiele & Kong (2018), but due to sparser observations, the correlation is not as tight as seen in this work. The trend observed by Mereminskiy et al. (2018) resembles the correlation observed for GRS 1915+105 (Shaposhnikov & Titarchuk 2007). Such correlation has been previously observed in several BHBs (Vignarca et al. 2003) and provides a tight link between the QPO and the hard-component emission. In that work, the correlation was found on time-scales of minutes in GRS 1915+105 and on scales of days-months for other transient BHBs. Here, we follow the QPO over 5 d. Fürst et al. (2016) also observe an extremely tight correlation of the QPO centroid frequency and power-law index in GX 339–4 in the frequency range of 0.6–1 Hz and Γ of 1.66–1.8. The authors estimate the mass of the BH using a scaling relation provided by Shaposhnikov & Titarchuk (2007).

The typical evolution of the outburst of a transient BHB is described best in the HID, where a counterclockwise path is followed. In the right 'vertical' branch, corresponding to the LHS, the flux increases, the power-law index is well correlated with it and the frequencies of the timing features, although no peaked QPO is usually observed, also increase (see Motta, Belloni & Homan 2009; Motta et al. 2011). Since the spectrum gradually softens, this branch is not really vertical. In the top 'horizontal' branch, the spectrum softens further, with the power-law index Γ increasing in absolute value. The flux usually continues to increase, although not as fast as before, and the QPO frequency is correlated with both flux and Γ. Given the shape of the PDS and the values of the power-law index, our observations are clearly on the HIMS branch. As described before, usually both the LHS and HIMS branches see a correlation between frequencies of variability components, the flux, and the power-law index. In our *AstroSat* data, we see the absence of a correlation with flux, although in the NICER data following our observation this correlation is present. This clearly shows that the QPO frequency is related to the energy spectral shape and not to the flux in either of the two main components. In a thermal-Comptonization scenario, the index of the hard component steepens as the population of electrons cools due to the increase in soft photon input (see e.g. Motta et al. 2009). However, from Fig. 4 we can see that this is not the case here, as the secular increase in disc flux is not followed by Γ. Another parameter that determines Γ is the optical depth of the cloud τ_0: for a spherical cloud and input photon energy much lower than the temperature of the electron cloud kT_e, we have $\Gamma = -1/2 + \sqrt{9/4 + \gamma}$, where $\gamma = \frac{\pi^2}{3}\frac{m_e c^2}{kT_e(\tau_0+2/3)^2}$ (Sunyaev & Truemper 1979; Sunyaev & Titarchuk 1980). Therefore in order to keep Γ from varying when the cloud temperature decreases is to increase τ_0 in a very specific way. Fluctuations in this relation could in principle give rise to the observed fluctuations in Γ, but it would be very ad hoc.

Within the model that associates the low-frequency QPO with Lense–Thirring precession of the inner part of the accretion flow (see Ingram & Done 2011; Ingram 2016, and references therein) the QPO frequency is related to the size of the inner flow portion that precesses. With increasing accretion rate, this region becomes smaller and the frequency increases. In our case, if the flux is a proxy for accretion rate, then this does not work. The same can be said of the Transition-Layer model (see Titarchuk & Fiorito 2004; Shaposhnikov & Titarchuk 2009), where also QPO frequency is related to accretion rate. Xu et al. (2017) attribute the increase of the QPO frequency to the inward motion of the inner accretion edge, which they test by comparing the QPO frequency with the inner truncation radius obtained from the spectral fitting. The inner hot component being optically thin could explain the non-thermal emission observed in MAXI J1535–571.

The correlation between the QPO frequency and the power-law index is observed to be tighter than the correlation between the QPO frequency and the flux in the duration of the *AstroSat* observation. The correlation between QPO frequency and flux picks up subsequent to the *AstroSat* observation. The strong correlation we observe implies that the fluctuations manifesting as QPOs are closely related to the Comptonizing region as opposed to typical models, assuming the origin of QPOs in the accretion disc.

In conclusion, the ν_{QPO}–Γ relation, which is a common property of the hard states of BHBs (LHS and HIMS), appears here more complex than previously known, and its origin must be investigated in detail, as none of the current models appear to be able to reproduce the results of this observation.

ACKNOWLEDGEMENTS

This work makes use of data from the *AstroSat* mission of the Indian Space Research Organisation (ISRO), archived at Indian Space Science Data Centre (ISSDC). The authors would like to acknowledge the support from the LAXPC Payload Operation Center (POC) and SXT POC at the TIFR, Mumbai for providing support in data reduction. YB acknowledges the help of his colleagues in understanding the *AstroSat* data. This work has been supported by the Executive Programme for Scientific and Technological cooperation between the Italian Republic and the Republic of India for the years 2017–2019 under project IN17MO11 [INT/Italy/P-11/2016 (ER)]. TMB acknowledges financial contribution from the agreement ASI-INAF n.2017-14-H.0.

REFERENCES

Antia H. M. et al., 2017, ApJS, 231, 10
Belloni T., 2005, in Burderi L., Antonelli L. A., D'Antona F., di Salvo T., Israel G. L., Piersanti L., Tornambè A., Straniero O., eds, AIP Conf. Proc. Vol. 797, Interacting Binaries: Accretion, Evolution, and Outcomes. Am. Inst. Phys., New York, p. 197
Belloni T., Psaltis D., van der Klis M., 2002, ApJ, 572, 392
Belloni T. M., 2010, in Belloni T., ed., The Jet Paradigm, Lecture Notes in Physics, Vol. 794. Springer-Verlag, Berlin, p. 53
Belloni T. M., Stella L., 2014, Space Sci. Rev., 183, 43
Belloni T. M., Motta S. E., Muñoz-Darias T., 2011, Bull. Astron. Soc. India, 39, 409
Casella P., Belloni T., Stella L., 2005, ApJ, 629, 403
Dinçer T., 2017, Astron. Telegram, 10716, 1
Done C., Gierliński M., Kubota A., 2007, A&AR, 15, 1
Fürst F. et al., 2016, ApJ, 828, 34
Gendreau K. et al., 2017b, Astron. Telegram, 10768, 1

Gendreau K., Arzoumanian Z., NICER Team, 2017a, American Astronomical Society Meeting Abstracts #229, p. 309.03
Ingram A., Done C., 2011, MNRAS, 415, 2323
Ingram A. R., 2016, Astron. Nachr., 337, 385
Kennea J. A., 2017, Astron. Telegram, 10731, 1
Kennea J. A., Evans P. A., Beardmore A. P., Krimm H. A., Romano P., Yamaoka K., Serino M., Negoro H., 2017, Astron. Telegram, 10700, 1
Markwardt C. B., Burrows D. N., Cummings J. R., Kennea J. A., Marshall F. E., Page K. L., Palmer D. M., Siegel M. H., 2017, GRB Coordinates Network, 21788, 1
Mereminskiy I. A., Grebenev S. A., 2017, Astron. Telegram, 10734, 1
Mereminskiy I. A., Grebenev S. A., Prosvetov A. V., Semena A. N., 2018, Astron. Lett., 44, 378
Motta S., Belloni T., Homan J., 2009, MNRAS, 400, 1603
Motta S., Muñoz-Darias T., Casella P., Belloni T., Homan J., 2011, MNRAS, 418, 2292
Negoro H., et al., 2017a, Astron. Telegram, 10699, 1
Negoro H. et al., 2017b, Astron. Telegram, 10708, 1
Russell T. D., Miller-Jones J. C. A., Sivakoff G. R., Tetarenko A. J., Jacpot Xrb Collaboration, 2017, Astron. Telegram, 10711, 1
Scaringi S., ASTR211 Students, 2017, Astron. Telegram, 10702, 1
Shaposhnikov N., Titarchuk L., 2007, ApJ, 663, 445
Shaposhnikov N., Titarchuk L., 2009, ApJ, 699, 453
Singh K. P., et al., 2014, in Space Telescopes and Instrumentation 2014: Ultraviolet to Gamma Ray, SPIE, Quebec, Canada. p. 91441S
Singh K. P. et al., 2017, J. Astrophys. Astron., 38, 29
Sreehari H., Ravishankar B. T., Iyer N., Agrawal V. K., , Katoch T. B., Mandal S., Nand i A., 2019, MNRAS, 487, 1270
Sridhar N., Bhattacharyya S., Chandra S., Antia H. M., 2019, MNRAS, 487, 4221
Stella L., Vietri M., 1998, ApJ, 492, L59
Stella L., Vietri M., Morsink S. M., 1999, ApJ, 524, L63
Stiele H., Kong A. K. H., 2018, ApJ, 868, 71
Sunyaev R. A., Titarchuk L. G., 1980, A&A, 86, 121
Sunyaev R. A., Truemper J., 1979, Nature, 279, 506
Titarchuk L., Fiorito R., 2004, ApJ, 612, 988
Verner D. A., Ferland G. J., Korista K. T., Yakovlev D. G., 1996, ApJ, 465, 487
Vignarca F., Migliari S., Belloni T., Psaltis D., van der Klis M., 2003, A&A, 397, 729
Wilms J., Allen A., McCray R., 2000, ApJ, 542, 914
Xu Y. et al., 2017, ApJ, 851, 103
Xu Y. et al., 2018, ApJ, 852, L34
Yadav J. S., et al., 2016, Space Telescopes and Instrumentation 2016: Ultraviolet to Gamma Ray, SPIE, Edinburgh, p. 99051D

This paper has been typeset from a TEX/LATEX file prepared by the author.